



Contents lists available at ScienceDirect

## Cold Regions Science and Technology

journal homepage: [www.elsevier.com/locate/coldregions](http://www.elsevier.com/locate/coldregions)

# Investigating the thermophysical properties of the ice–snow interface under a controlled temperature gradient

## Part I: Experiments & Observations

Kevin Hammonds\*, Ross Lieb-Lappen, Ian Baker, Xuan Wang

Thayer School of Engineering at Dartmouth College, Hanover, NH, USA

## ARTICLE INFO

## Article history:

Received 7 November 2014  
 Received in revised form 23 July 2015  
 Accepted 4 September 2015  
 Available online xxx

## Keywords:

Ice lens  
 Ice crystal growth  
 Interface  
 Kinetic snow metamorphism  
 Temperature gradient  
 Micro-CT

## ABSTRACT

Of critical importance for avalanche forecasting, is the ability to draw meaningful conclusions from only a handful of field observations. To that end, it is common for avalanche forecasters to not only have to rely on sparse data, but also on their own intuitive understanding of how their field-based observations may be correlated to complex physical processes responsible for structural instability within a snowpack. One such well-documented basis for mechanical instability to increase within a snowpack is that caused by the presence of a buried ice lens or ice crust. Although such icy layers are naturally formed and frequently encountered in seasonal snowpacks, very little is known about the microstructural evolution of these layers and how they contribute toward weak layer development. Furthermore, in terms of assessing the structural integrity of the snowpack, there is at the present time no consistent treatment for identifying these layers a priori as problematic or benign. To address this issue, we have created an idealized laboratory scenario in which we can study how an artificially created ice lens may affect the thermophysical and microstructural state of the interface between the ice lens and adjacent layers of snow while under a controlled temperature gradient of primarily  $-100 \text{ K m}^{-1}$ . Utilizing in situ micro-thermocouple measurements, our findings show that a super-temperature gradient exists within only a millimeter of the ice lens surface that is many times greater than the imposed bulk temperature gradient. Such large temperature gradients on such a small scale would not be measurable by most field-based instrumentation and to our knowledge these laboratory-based in situ measurements are the first of their kind. Additionally, we have also investigated and characterized the microstructural evolution of the ice–snow interface with X-ray Micro-computed Tomography and Scanning Electron Microscopy. In our analysis, we have been able to identify distinct regions of simultaneous ice crystal growth, sublimation, and kinetic snow metamorphism. We hold that these observations are both consistent with previous laboratory studies and observations made in the natural environment.

© 2015 Elsevier B.V. All rights reserved.

## 1. Introduction

It has long-been observed in seasonal mountain snowpacks that it is often the natural formation of a snow or ice crust on the surface of the snowpack, that once buried, is responsible for dangerous and widespread avalanche conditions (Jamieson et al., 2001; Greene and Johnson, 2002). Crusts of nearly pure ice, termed ice lenses, can form from a variety of meteorological conditions including significant melt/freeze or freezing rain events (Fierz et al., 2009). Once formed, these ice lenses create both a sharp discontinuity in the thermal conductivity of the adjacent snow layers and a nearly impermeable barrier to the diffusion of water vapor through the snowpack (Adams and Brown, 1983;

Fierz, 1998; Colbeck and Jamieson, 2001). Additionally, ice lenses once buried can also persist throughout the entire winter season and act repeatedly as an ideal sliding surface for slab avalanches (Jamieson and Johnston, 1997). Although recent progress has been made in modeling many snowpack properties, such as the anisotropic thermal conductivity (Shertzer and Adams, 2011), small-scale temperature gradients across pore spaces (Kaempfer et al., 2005), and temperature gradient metamorphism of dry snow (Schneebeli and Sokratov, 2004), it remains unclear as to how these thermophysical properties and processes are related to the more disjointed situation of a buried ice lens within a snowpack. This may be in part due to the tumultuous nature of naturally-formed ice lenses and crusts, as they are rarely created in a uniform or predictable enough fashion to warrant an accurate representation when considering areas of scale. Without the aid of broad field-based data collection, such as perhaps could be derived from collocated snow penetrometer measurements (Marshall and Johnson, 2009; Löwe and Van Herwijnen, 2012), it will likely remain very difficult

\* Corresponding author at: Ice Research Laboratory, Thayer School of Engineering at Dartmouth College, 14 Engineering Drive, Hanover, NH 03755, USA. Tel.: +1 603 646 6511 (office); +1 970 481 2745 (mobile).

E-mail address: [kevin.d.hammonds.th@dartmouth.edu](mailto:kevin.d.hammonds.th@dartmouth.edu) (K. Hammonds).

to estimate and parameterize the natural variability in the porosity, permeability, tortuosity, and thickness of such ice layers and crusts. Further compounding the issue, the same local variability also exists for the snow layers adjacent to the ice lens (Schweizer et al., 2008). Nevertheless, because these ice lenses have been linked to widespread avalanche activity in the past, it seems prudent to not overlook such a clear relationship of cause and effect. In this paper, we present a new and systematic laboratory approach to better understanding the thermophysical properties and processes taking place at the ice–snow interface. Using primarily an imposed steady state temperature gradient of  $-100 \text{ K m}^{-1}$ , our laboratory technique involves both the time-dependent microstructural characterization of the ice–snow interface as well as the measurement of in situ temperature gradients from within 1 mm of the interface. In characterizing the microstructure, we documented the temporal evolution of the interface at 6 h intervals over a 48 h testing period using X-ray Micro-computed Tomography ( $\mu$ -CT) and performed post-test analysis via Scanning Electron Microscopy. In order to capture sub-millimeter temperature gradients, we integrated a micro-thermocouple array into the housing of our laboratory prepared ice–snow samples. Obtaining these physical temperature measurements was a key objective of this work that we believe may also extend the findings of other previous studies related to the modeling of heat and mass transfer in dry snow (Kaempfer et al., 2005), modeling combined with  $\mu$ -CT observations of snow metamorphism (Flin and Brzoska, 2008; Pinzer et al., 2012), estimation of small-scale temperature gradients with laboratory and field-based thermal imaging (Shea et al., 2012; Schirmer and Jamieson, 2014), and in situ investigations on the thermal conductivity of dry snow (Riche and Schneebeli, 2013). Furthermore, we contend in our working hypothesis that the empirical observations correlating buried ice lenses to widespread avalanche activity and weak layer development are due to sub-millimeter scale thermophysical processes, and that these processes are related to sub-millimeter scale temperature gradients not previously recorded. All laboratory experiments were conducted in the Dartmouth Ice Research Laboratory (IRL) or the Dartmouth Electron Microscope Facility (EMF).

## 2. Background

### 2.1. Previous work

While several theoretical and laboratory studies have been conducted in the past to investigate heat and mass transfer mechanisms related to snow metamorphism (Kaempfer et al., 2005; Flin and Brzoska, 2008; Pinzer et al., 2012; Riche and Schneebeli, 2013; Wang and Baker, 2014) and snowpack stability (Adams and Brown, 1990; Colbeck, 1991; Fierz, 1998; Colbeck and Jamieson, 2001) few have been able to mesh the two. One study that did successfully combine both field and laboratory experiments, to which the work being presented here is closely related, was that of Greene (2007). In order to investigate the effects of buried ice lenses and crusts in a snowpack, Greene conducted a series of laboratory experiments with both naturally collected and artificially created ice lenses and crusts. After imposing an applied steady-state temperature gradient, Greene utilized a serial sectioning and three-dimensional reconstruction technique which allowed him to make several interesting observations indicative of an increase in the temperature gradient near these layers. Some of these observations included 1) vertical chains of faceted and hollow particles growing from the bottom (warmer) side of the ice lens, 2) sublimation and smoothing from the upper (cooler) surface of the ice lens, and 3) development of microcavities directly above the ice layer. In the end, however, Greene was not able to quantify the potential mechanisms responsible for these observations, citing that there was “no consistent signal from the ice layer in the temperature data”. Greene notes in his conclusions that some potential reasons for this may have been simply due to insufficient thermocouple sensitivity ( $\pm 0.5 \text{ K}$ ), too large of a distance between the thermocouple probes (1.0 cm), or thermocouple probes

that were too large in diameter ( $255 \mu\text{m}$ ). Greene also remarks that detecting occurrences of new ice crystal growth or sublimation at the ice–snow interface would be difficult with standard field techniques.

### 2.2. Thermophysical considerations

Within any homogeneous snowpack, it is the thermodynamic processes of both conduction and the release of latent heat that are generally responsible for the overall metamorphic state and resulting microstructure of the snowpack (Armstrong, 1985). In this sense, homogeneity is defined by the thermal conductivity remaining constant from point to point. Should there be any variation in the thermal conductivity, such as could be due to the introduction of a physical barrier or a change in the porosity, then the material would be inhomogeneous (Kakac and Yener, 1993). Mathematically, either relationship is best described by the three-dimensional heat equation as shown in Eq. (1), where  $\rho$  is taken to be the density,  $c_p$  is the specific heat capacity at constant pressure,  $\mathbf{q}$  the heat flux via conduction or latent heating,  $T$  the temperature of the conductive medium, and  $t$  the time over which the temperature is changing (Greene, 2007).

$$\rho c_p \frac{\partial T}{\partial t} = -\nabla \cdot (\mathbf{q}_{\text{conduction}} + \mathbf{q}_{\text{latent heat}}). \quad (1)$$

In this treatment we have chosen to neglect  $\mathbf{q}_{\text{convection}}$  based on the calculation of Grashof and Knudsen numbers, although it should be noted that large scale free convection has been observed in natural snowpacks (Sturm and Johnson, 1991) and in other laboratory experiments under very large temperature gradients ( $\geq 500 \text{ K m}^{-1}$ ) and high permeability snow types (Akitaya, 1974; Powers et al., 1985).

#### 2.2.1. Grashof number

The thermal variant of the Grashof number  $Gr_L$ , a dimensionless parameter commonly encountered in heat and mass transfer problems, is the ratio of buoyancy forces to viscous forces that would be required for a thermally convective boundary layer to exist via purely free convection (Bergman et al., 2011). In this study, we use a more general variation of the Grashof number  $Gr_C$ , in which both mass and heat transfer are included (Bergman et al., 2011). This allows for concentration gradients, such as water vapor in air, to also be considered for free convection. The potential for free convection to occur at an interface is generally thought to be important when  $Gr_L \geq 1000$  (Holman, 2002; Greene, 2007), but it should be noted that the significance of  $Gr_L$  or  $Gr_C$  is heavily dependent on flow direction, geometry, and the characteristic length selected (Levenspiel, 1998). Both  $Gr_L$  and  $Gr_C$  are given in Eqs. (2) and (3), respectively, where  $g$  is the acceleration due to gravity,  $\beta$  is the volume coefficient for expansion of the fluid,  $\Delta T_c$  is the temperature difference between the surface and the edge of the boundary layer ( $\Delta T_c = T_s - T_\infty$ ),  $L_c$  is the characteristic length,  $\nu_f$  is the kinematic viscosity of the fluid,  $\rho_f$  is the density of the fluid,  $\Delta \rho_c$  is the difference in the fluid density between the surface and the edge of the boundary layer ( $\Delta \rho_c = \rho_s - \rho_\infty$ ), and  $\nu_j$  is the kinematic viscosity of the fluid (Bergman et al., 2011).

$$Gr_L = \frac{g\beta\Delta T_c L_c^3}{\nu_f^2} \quad (2)$$

$$Gr_C = \frac{g\Delta \rho_c L_c^3}{\rho_f \nu_f^2} \quad (3)$$

In these equations, the cubic exponent on  $L_c$  gives a particular significance to how  $L_c$  is determined. The selection of  $L_c$  is typically defined in heat and mass transfer problems as the ratio of the solid's volume to surface area, thickness of a plane wall separating two fluids, or the ratio of the surface area to the perimeter of the solid (Bergman et al., 2011). Fig. 1 demonstrates this significance, where  $L_c$  has been plotted

as a function of  $\Delta T_c$  for both  $Gr_L$  and  $Gr_C$  equal to 1000. For comparison in this plot,  $\Delta\rho_c$  has been recast as  $\Delta T_c$ , which shows that when using the more general form of the Grashof number  $Gr_C$ , the necessary  $L_c$  for free convection is decreased. Based on  $L_c$  in this figure, a convective cell proportional in size to the diameter of our specimen would be required for free convection to occur. Given that snow is a porous medium, this seems highly unlikely, as the porous nature of snow would only further restrain the possible values for  $L_c$ . Greene, 2007 came to a similar conclusion based on  $Gr_L$ , but did not explicitly consider  $Gr_C$ .

### 2.2.2. Knudsen number

In evaluating the significance of a convection term in Eq. (1), the length scale of the physical processes to be studied should also be taken into consideration. Recent works on micro-scale (<1 mm) heat transfer processes have shown that deviations are possible from the predictions of a continuum heat transfer theory (Sobhan and Peterson, 2008; Ghiaasiaan, 2011), when the size of the physical domain under consideration becomes important due to the prevalence of molecule–molecule interactions vs. molecule–wall interactions. Understanding these micro-scale mechanisms of heat transfer remains a very active area of research (Sobhan and Peterson, 2008) and although we do not address micro-scale heat transfer explicitly, we do assess the relevance of micro-scale influences based on the calculation of the Knudsen number  $Kn$ , which is the ratio of the molecular mean free path  $\lambda_{mol}$  of the gas to the characteristic length of the flow field (Ghiaasiaan, 2011), given in Eq. (4).

$$Kn = \frac{\lambda_{mol}}{L_c} \quad (4)$$

For porous mediums, the characteristic length can be considered restrained by the pore size and thus similar to that of the Grashof number. For  $Kn \leq 10^{-3}$ , conventional continuum treatments of heat transfer may be applied (Ghiaasiaan, 2011). For air at 288 K and 100% relative humidity,  $\lambda_{mol} = 63.8$  nm (Jennings, 1988), and Fig. 2 shows the minimum characteristic lengths for which  $Kn \leq 10^{-3}$ . In Fig. 2, micro-scale effects do not become relevant until pore diameters shrink to well below 50  $\mu\text{m}$  in diameter.

## 3. Methods

### 3.1. Sample preparation

Following Cole (1979), we created polycrystalline specimens of pure ice. These cylindrical specimens were then cut with a precision band saw to the desired thickness (2 mm, 4 mm, or 8 mm). An example of

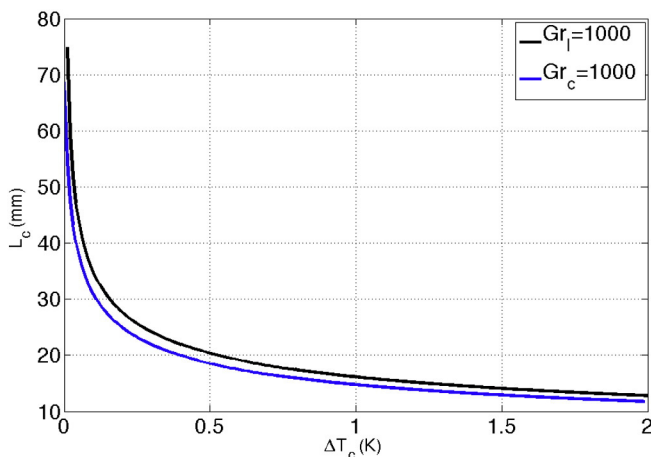


Fig. 1. Characteristic length necessary over a temperature difference of 2 K for  $Gr_L$  and  $Gr_C$  equal to 1000.

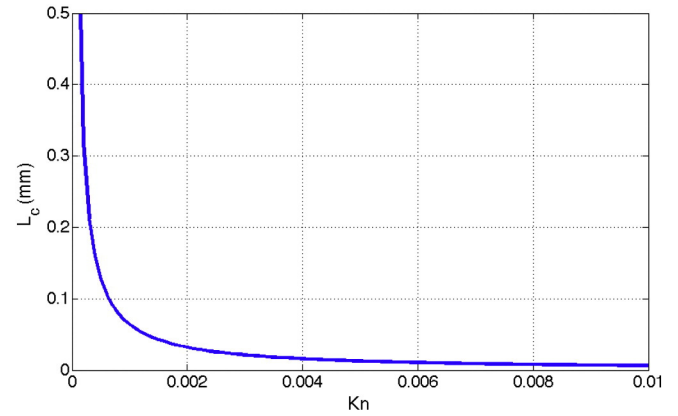


Fig. 2. Characteristic length  $L_c$  of minimum pore size for which a continuum heat transfer treatment is applicable based on Knudsen number calculations.

a typical ice lens, when viewed through crossed polarizing filters, is shown in Fig. 3. Ice lenses were placed between two layers of old (>1 yr.) naturally collected snow that has been kept at an isothermal temperature of  $-10$  °C. The old snow had a grain size of 2.5–3 mm, was rounded in character, and had a density of approximately  $300 \text{ kg m}^{-3}$ . Our ice–snow sample was housed in a 50 mm tall  $\times$  20 mm diameter (17 mm inner-diameter) polycarbonate tube with press-fit copper caps of 4 mm thickness. The tube was designed and machined to seal the ice–snow sample from any exterior influences other than that of the imposed temperature gradient. The tube itself was then placed in an insulated sleeve of polystyrene foam before being loaded into the temperature gradient controlling apparatus. Less the polystyrene insulation, an example of an ice–snow specimen containing a 2 mm thick ice lens is shown in Fig. 4.

### 3.2. Temperature gradient apparatus

The temperature gradient was controlled by two Electron peltier modules (model # TEC1-12707HT), with an accuracy of  $\pm 0.1$  K, that were kept in flush contact with the copper caps of the specimen. Temperatures at the end caps were monitored with type-T Omega surface thermocouples (model #SA1XL-T-SRTC). The temperature gradient controlling apparatus was housed in a cold room kept at 263 K. This was the same room used to house the  $\mu\text{-CT}$ , such as to limit the amount of time that the sample would be out of the temperature gradient controlling apparatus while being scanned. For all experiments, a unidirectional and steady-state temperature gradient of  $-100 \text{ K m}^{-1}$  was applied. This equated to a temperature at the top and bottom of the sample of

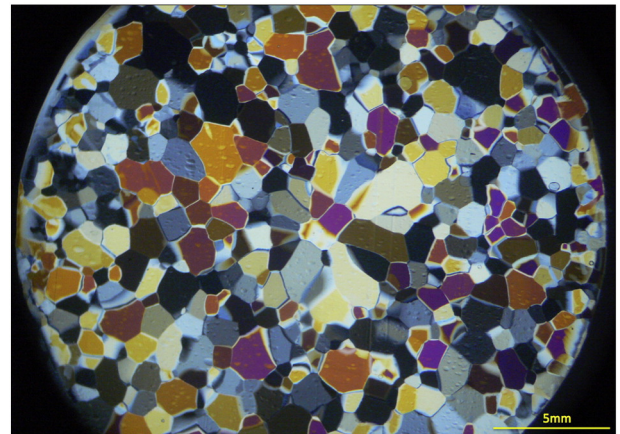


Fig. 3. Polycrystalline ice lens as viewed through crossed polarizing filters.



Fig. 4. Ice–snow sample with a 2 mm thick ice lens placed between natural snow with a grain size of 2.5–3 mm.

260.85 K and 265.25 K, respectively. These temperatures were chosen in an effort to best represent the observed conditions often present near the surface of winter mountain snowpacks (Birkeland et al., 1998), where large temperature gradients of  $-100 \text{ K m}^{-1}$  or greater can occur (Birkeland et al., 1998; McClung and Schaerer, 2006).

### 3.3. Time-lapse X-ray Micro-computed Tomography

Once under a constant temperature gradient, our ice–snow sample was imaged every 6 h over a 48 h period via  $\mu$ -CT. This includes a 0 h scan for a total of 9 scans per test. We used a Skyscan 1172 housed in a 263 K cold room in the IRL. A 40 kV, 250 mA X-ray beam was chosen and the sample was rotated  $180^\circ$  at  $0.7^\circ$  increments while being scanned. Attenuation profiles were captured using a 1.3 Mp, 12-bit, cooled CCD Hamamatsu camera. This allowed for a  $15 \mu\text{m}$  resolution to be obtained over a total scanning period of less than 20 min. Experiments were repeated for a 2 mm, 4 mm, or 8 mm ice lens and a  $-100 \text{ K m}^{-1}$  temperature gradient. Image post-processing and three-dimensional image reconstruction were performed using NRecon software, and included thermal drift correction, post alignment, removal of ring artifacts, Gaussian pixel smoothing, and beam hardening correction. The resulting images were on a 0–255 grayscale, and then binarized into snow and air phases by selecting the appropriate threshold, the same threshold being used for all experiments. Following each scan, a detailed analysis of the 1.5 mm above and below the ice lens was performed, resulting in 100 horizontal cross-sectional images for both above and below the ice lens. To filter out any additional noise due to edge effects or inadvertent tilting of the 20 mm circular diameter sample while in the  $\mu$ -CT, analysis was only performed on the inner 14 mm diameter volume.

### 3.4. Scanning Electron Microscopy

At the end of each 48 h  $\mu$ -CT scanning period, ice–snow samples were removed from the polycarbonate tube and examined using a field emission gun FEI XL30 scanning electron microscope (SEM), equipped with a Gatan cryotransfer/cooling system. Both surfaces of

the ice lens were imaged in secondary electron (SE) mode while on a cold stage maintained at 173 K. A 15 kV acceleration voltage was used and significant charging was observed. A lower acceleration voltage of perhaps 2 kV is recommended for future work (Chen and Baker, 2010).

### 3.5. In situ micro-thermocouple measurements

In order to physically capture the sub-millimeter scale temperature gradient at the ice–snow interface, we modified the housing of our ice–snow samples used for  $\mu$ -CT observations by square milling the face of the polycarbonate tube into a flat surface and drilling a series of 12 holes at specific locations with a high precision ( $10 \mu\text{m}$  accuracy) mill in the machine shop. Each hole had a diameter of  $360 \mu\text{m}$ , which allowed for the hand placement of our  $79 \mu\text{m}$ , type-T Omega Precision Fine Wire thermocouples (model # 5SC-TT-T-40-36). Once placed, these thermocouples were held in position with electrical tape, as shown in Fig. 5, but were then also wrapped with a secondary layer of electrical tape to assure an adequate seal. The location of the thermocouples was chosen such that we would obtain two measurements out in the bulk snow below the ice lens, four measurements within 1 mm immediately below the ice lens, four measurements from within 1 mm immediately above the ice lens, and two measurements in the bulk snow above the ice lens, for a total of 12 in situ temperature measurements around a 4 mm ice lens. The holes were drilled in a linear array, with the exception of the holes directly above and below the ice lens, which were horizontally staggered at  $200 \mu\text{m}$  intervals to accommodate a total spacing of  $600 \mu\text{m}$  when measured from the center of each hole. In an effort to ensure uniform spacing, each thermocouple was placed against the edge of each hole, but we believe that some variability of the location of each thermocouple may exist and that the actual linear dimension of the total thermocouple spacing may have varied up to a maximum of 1 mm. For this reason, we use a value of  $800 \pm 200 \mu\text{m}$  in our temperature gradient calculations near the ice lens.

Once an ice–snow sample was loaded and micro-thermocouples were appropriately positioned, the sample was placed in the same temperature gradient controlling apparatus as was used for the  $\mu$ -CT observations. Temperatures were logged at 10 s intervals over a 24 h time period using an Omega RDXL12SD datalogger. An initial temperature gradient of  $-100 \text{ K m}^{-1}$  was used and steady state heat flow was achieved. Using the same sample, the temperature gradient was then successively decreased to  $-50 \text{ K m}^{-1}$ ,  $-10 \text{ K m}^{-1}$ , and  $-4 \text{ K m}^{-1}$ , also held for 24 h each. For all temperature gradients, the temperature at the bottom of the sample was held constant at 265.45 K, while the temperature at the top of the sample was stepped up sequentially (260.85 K, 263.15 K, 264.95 K, 265.25 K). In order to calibrate the experiment without removing and potentially changing the location of the

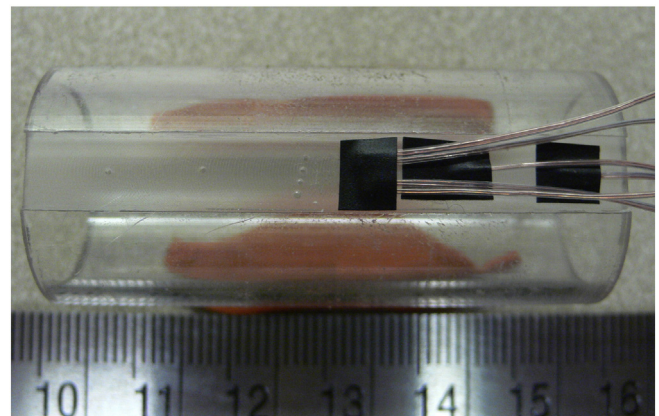


Fig. 5. Photograph of micro-thermocouple placement in the machined polycarbonate tube.

micro-thermocouples, at the end of the temperature gradient experiment, the ice–snow sample was removed from the cold room and allowed to melt. The same polycarbonate tube with the thermocouples still in place was then reloaded with snow grains of approximately the same bulk density and no ice lens. The experiment described above was then repeated and these measurements served as calibration for a purely linear temperature gradient.

## 4. Results

### 4.1. $\mu$ -CT observations

Overall, our  $\mu$ -CT observations were consistent with those made by Greene (2007). For each experiment, we observed faceted ice crystal growth from the bottom side of the ice lens while the top remained relatively smooth. The new ice crystals were estimated to be on the order of 0.5 mm in length, as recorded at the termination of each test. Kinetic snow metamorphism was also observed to be occurring as the snow grains adjacent to the ice lens sequentially became more faceted and smaller in size. An example time-lapse sequence in which a 2 mm ice lens was used is shown in Fig. 6. It should be noted when viewing this figure, however, that the images were not taken from the same viewing angle and therefore should not be construed as also showing the metamorphism of individual snow grains. As per the development of micro-cavities above the ice lens, we could not identify these directly, but this may be due to the rather large snow grains we used in our experiments when compared to Greene (2007). Less apparent in Fig. 6, we also observed a preference for this new ice crystal growth to occur along the ridged sections of the ice lens. More clearly seen from an orthogonal viewing angle along the z-axis just near the bottom face of a 2 mm ice lens, as shown in Fig. 7, deposition upon the ice lens has occurred where a striated and ridged pattern was left behind by the band saw. Somewhat expected and also observed for natural ridges in Greene (2007), this patterning is most likely due to the higher surface energy and consequently lower contact angle needed for heterogeneous nucleation to occur at these ridged sections of the ice lens (Pruppacher and Klett, 1997). Lastly, we also observed an interesting wave-like character to exist along the top surface of the ice lens, while voiding seems to have

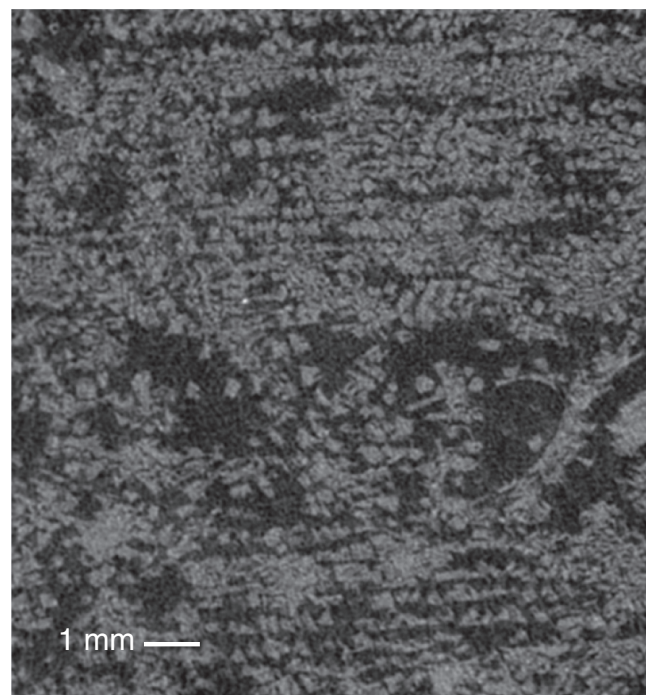


Fig. 7.  $\mu$ -CT image of the bottom face of an ice lens showing striated preferential ice crystal growth in the image along the “ridged” sections (left to right in the image) of the ice lens after being exposed to a  $-100 \text{ K m}^{-1}$  temperature gradient for 48 h.

occurred along the bottom surface. These features are best viewed using a  $\mu$ -CT animation of a 48 h scan and a 2 mm ice lens, which can be viewed in the Supplementary Data of Appendix A. When following these waves around the outer edge of the ice lens, they seem to have a semi-regular and periodic signature. It is unclear whether or not these waves have originated via sublimation from the same band saw patterning as previously described or are a physical manifestation of some other thermophysical process. Similarly, along the bottom surface

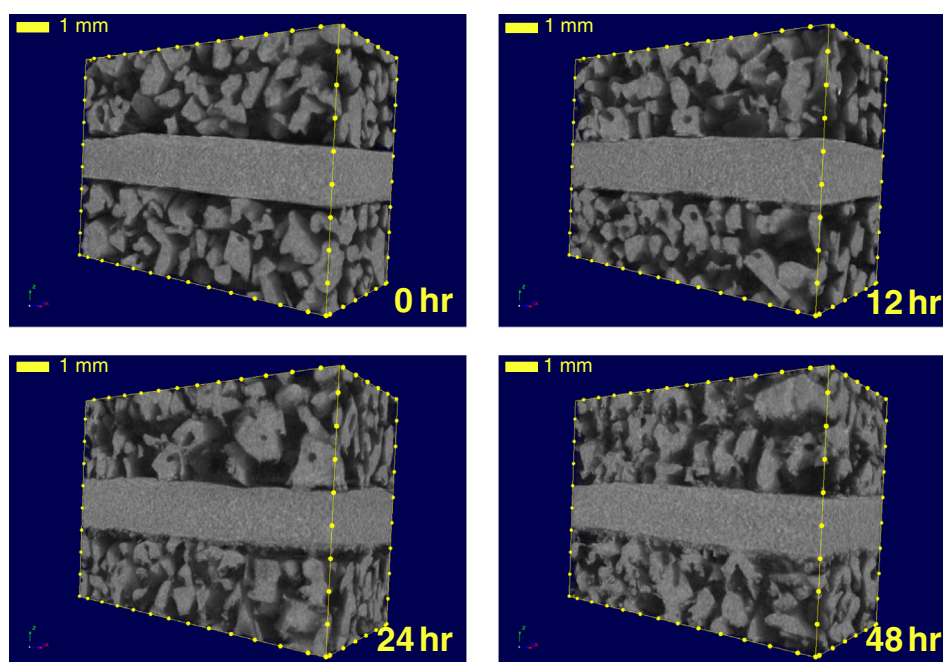


Fig. 6. Time lapse  $\mu$ -CT reconstructions of a 2 mm thick ice lens evolving under a constant temperature gradient of  $-100 \text{ K m}^{-1}$  over a 48 h period. Shown here are the 0, 12, 24, and 48 h images.

of the ice lens, there were irregular concavities that had developed. Because new ice crystal growth was still observed to be occurring within these concavities, however, it is difficult to say if they were present beforehand in the experiment or were developed at a later time.

#### 4.2. $\mu$ -CT analysis

##### 4.2.1. Mean grain diameter

In our quantitative  $\mu$ -CT analysis, we chose to focus on the three parameters that demonstrated the most consistent trends across all of our experiments and could be linked to physical processes. These parameters were the mean grain diameter  $D_m$ , the connectivity density  $\rho_{conn}$ , and the specific surface area (SSA). For each test, these parameters were calculated for the 1.5 mm tall by 14 mm diameter volume of interest (VOI) above and below the ice lens. Shown in Fig. 8, where the solid and dashed lines are the best linear fits via least squares fitting to the data points, it can be observed that  $D_m$  decreased at a much faster rate below the ice lens than that above. Upon physical inspection of these snow grains, it was determined that the large volume of new ice crystal growth in this region was responsible for the steeper decrease in  $D_m$  when considering the entire VOI. With regard to the overall decreasing trend in  $D_m$ , we attribute this to the initial conditions of large snow grains and a large applied temperature gradient. Further, we would not necessarily expect all snow types to grow smaller, given the same conditions.

##### 4.2.2. Connectivity density

The presence of a signal in our data from the new ice crystal growth was not limited to  $D_m$ , but was also observed in  $\rho_{conn}$ . Shown in Fig. 9,  $\rho_{conn}$  displays a signal of the new ice crystal growth, as a much larger increase in  $\rho_{conn}$  is observed below the ice lens when compared to above. This would indicate that the ice lens itself is becoming more connected to the snow layer below, which may have important consequences for predicting conductive heat flow as the number of conductive pathways is being increased between the two materials. For a porous medium, such as snow, we would then also expect to see a decrease in the porosity for this region.

##### 4.2.3. Specific surface area

In evaluating the SSA, we were able to delineate between the regions of new ice crystal growth and existing snow grain metamorphism in our

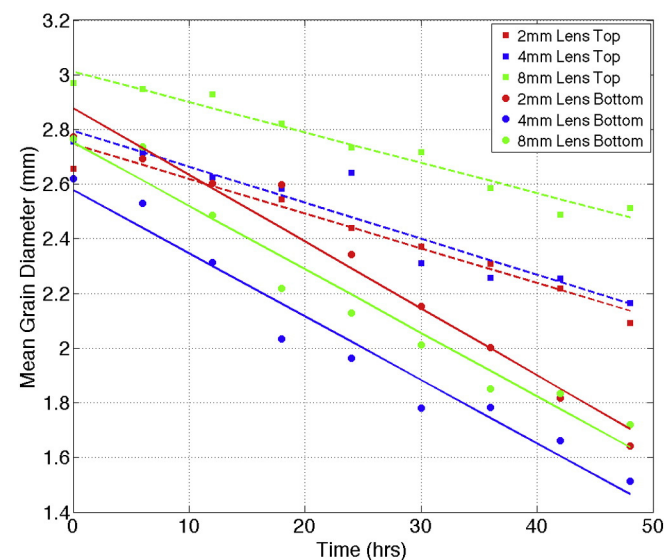


Fig. 8. Evolution of the mean grain diameter over a 48 h period and  $-100 \text{ K m}^{-1}$  applied temperature gradient. The same VOI was used for above (dashed) and below (solid) each ice lens.

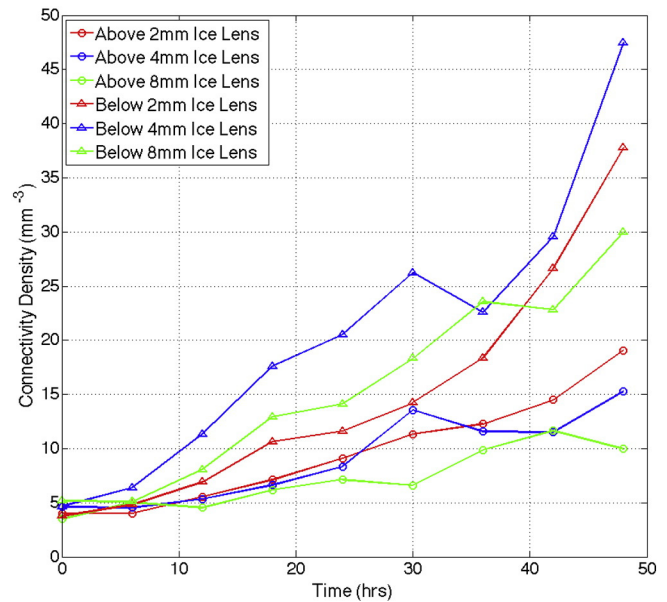
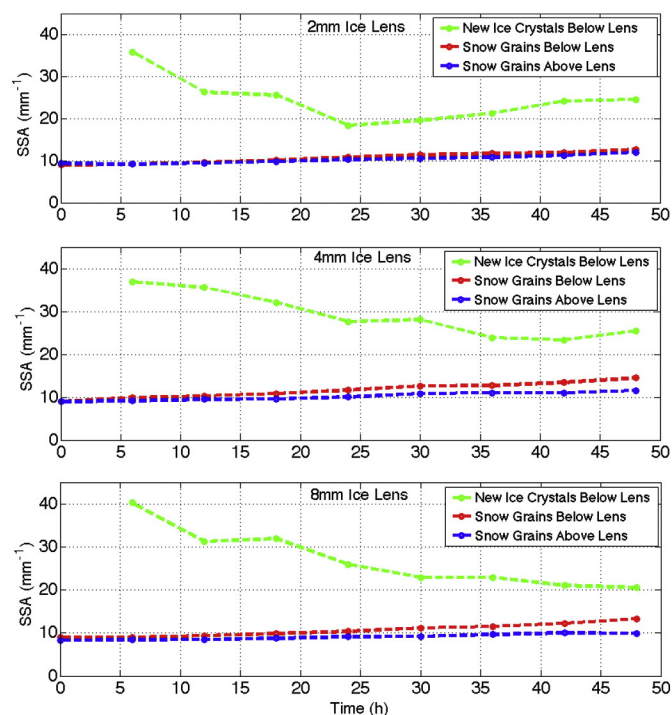


Fig. 9. Evolution of the connectivity density over a 48 h period and  $-100 \text{ K m}^{-1}$  applied temperature gradient. The same VOI was used for above and below each ice lens.

analysis. This was done by estimating the ice crystal growth rate normal to the bottom of the ice lens and allowing for this estimate to dictate the number of horizontal cross-sectional images that would then be binned into either a region of “new growth” or “snow grain metamorphism”. This sequential binning approach provided a much more dynamic view of our time-lapse observations that allowed us to track and analyze the SSA in each region independently. Binning above the ice lens was not necessary and it was assumed that any changes in  $D_m$ ,  $\rho_{conn}$ , or the SSA in this region would have been only due to snow grain metamorphism. Shown in Fig. 10, are a series of plots corresponding to the calculated SSA for each individual experiment and VOI, both binned and static. Overall, the initial SSA is roughly the same for all experiments and there is a slight increase in the SSA of the snow grains both above and below each ice lens. We interpret this trend as indicative of kinetic snow metamorphism and a reduction in the volume and diameter of the snow grains. Similarly, we would not expect a dramatic difference in snow grain metamorphism on either side of the ice lens as both sides are experiencing similar magnitudes in the temperature gradient. As per the binned region of newly formed ice crystal growth, there is an overall decrease, but with an inflection point that appears most exaggerated in the data from the 2 mm ice lens experiment. This point of inflection could be due to something simple, such as our moving VOI not correctly capturing the new ice crystal growth independent of the adjacent snow grains, but if this were the case you would also expect to see similarly timed inflection point in the SSA for the snow grains. Alternatively, it could be linked to something more complex, such as the newly formed ice crystals reaching some sort of critical dimension in which they begin to experience a shift in growth regimes, perhaps becoming more epitaxial in nature. Further investigation of this is beyond the scope of this paper. Instead, we focus our attention on interpreting the overall decrease in the trend of the SSA for the new ice crystal growth region before these inflection points, which is likely due to the volume of the newly formed ice crystals increasing at a faster rate than the surface area. This trend would be indicative of step-wise lateral crystal growth (Hobbs, 1974), and may be further evidenced with SEM analysis.

##### 4.2.4. Porosity

In our calculations of the porosity, shown in Fig. 11, we looked at four different regions above and below the ice lens. Similar to the SSA,



**Fig. 10.** SSA for the 2 mm, 4 mm, and 8 mm ice lens cases, while under an imposed temperature gradient of  $-100 \text{ K m}^{-1}$ . Dashed green lines represent the newly formed ice crystal growth on the bottom of the ice lens, while dashed blue and red lines represent the snow grains above the ice lens and below the region of new ice crystal growth, respectively. (For interpretation of the references to colors in this figure legend, the reader is referred to the web version of this article.)

we tracked just the region of new ice crystal growth below the ice lens, where we observed relatively high initial porosity's of around 70–80% followed by a steady decrease that seemed to stabilize near 60% porosity. When compared to the remainder of the snow grains below this dynamic region of new ice crystal growth, which remained steady at 50–55% porosity, this value is approximately 5–10% larger on average. Directly above the ice lens, we compared a static VOI of 0.3 mm in height to the total VOI as before in our other  $\mu$ -CT calculations. These results show that while the porosity in the 0.3 mm region remained stable over time, it was typically 5% greater than that of the total VOI for the snow grains above the ice lens and 5% less than the porosity of the dynamic region of new ice crystal growth below the ice lens. Similar to  $\rho_{\text{conn}}$ , these differences in the porosity near the ice–snow interface could have a significant effect on the observed temperature gradient as higher values in the porosity would imply fewer connections between the snow grain structure and the ice lens.

#### 4.3. SEM observations

In our SEM analysis, our observations were generally consistent with the microstructural characteristics already described in the previous section. Some additions include that 1) although other orientations were also observed, the new ice crystal growth appeared to have a preference for its a-axis orientation to be perpendicular to that of the ice lens and 2) that the clear visibility of grain boundaries upon the top surface of the ice lens demonstrates the apparent smoothness of this surface. Shown in Fig. 12, is a select number of SEM images that illustrate these and the previously discussed characteristics pertaining to the ice lens and adjacent snow grains at the end of each 48 h experiment. When comparing the difference between Fig. 12a–c (for the 2 mm, 4 mm, and 8 mm ice lenses) it would appear that the new ice crystal growth upon the 8 mm ice lens is much more faceted and

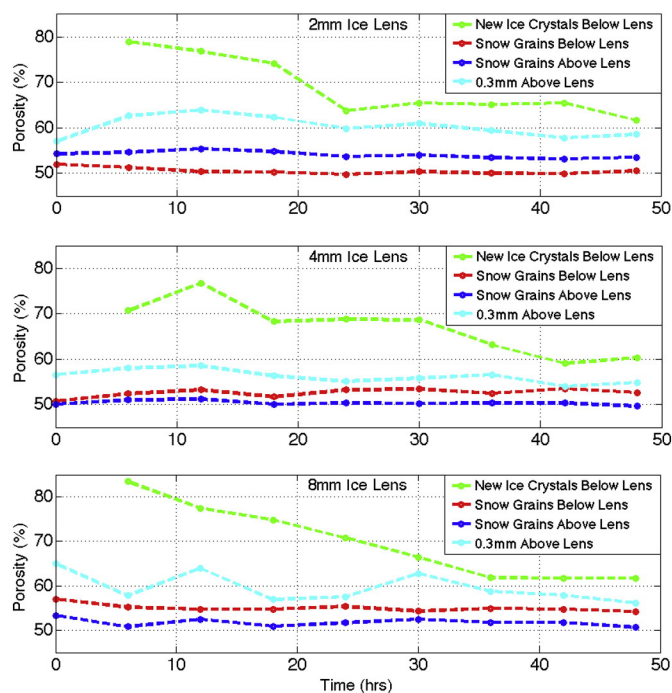


**Fig. 11.** Porosity for the 2 mm, 4 mm, and 8 mm ice lens cases, while under an imposed temperature gradient of  $-100 \text{ K m}^{-1}$ . Dashed green lines represent the region of newly formed ice crystal growth on the bottom of the ice lens, dashed cyan the static 0.3 mm region above the ice lens and dashed blue and red lines represent the snow grains above the ice lens and below the region of new ice crystal growth, respectively. (For interpretation of the references to colors in this figure, the reader is referred to the web version of this article.)

sharply cornered than the 2 mm ice lens. This may be due to a difference in the surface heating effects associated with the release of latent heat upon deposition (Libbrecht, 2004), where the 8 mm ice lens was most likely able to conduct away heat more efficiently than the 2 mm ice lens. Also, it should be noted that Fig. 12d was in general characteristic of multiple magnifications and that the faceted snow grain in Fig. 12e was taken from the top surface of an 8 mm ice lens with the faceted structure facing downward toward the ice lens.

#### 4.4. Micro-thermocouple measurements

Micro-thermocouple measurements from the first 24 h period of an applied temperature gradient of  $-100 \text{ K m}^{-1}$  yielded very interesting results. Shown in Fig. 13a is the measured temperature gradient (red) and representative bulk linear temperature gradient (blue) for comparison. For reference, this figure has also been overlaid by a schematic representation of the ice lens and ice–snow sample housing as well as red vertical hash bars to indicate the inherent error of the micro-thermocouple measurements. Immediately discernable in Fig. 13a and magnified in Fig. 13b, are two very significant deviations of the measured temperature gradient from the linear temperature gradient just above and below the ice lens. These measurements equate to a temperature gradient of approximately  $-300 \text{ K m}^{-1}$  above the ice lens and  $-650 \text{ K m}^{-1}$  below the ice lens when calculated using a difference in height  $\Delta z$  of  $800 \mu\text{m}$  (see Section 3.5). These values are quite large when compared to the linear temperature gradient shown, which was simply drawn and calculated between the two outermost thermocouple measurements and equates to only  $-115 \text{ K m}^{-1}$ . It is not exactly clear why the  $-100 \text{ K m}^{-1}$  temperature gradient imposed on the sample was not more closely followed, but it may have been due to a thin air gap that formed between the bottom of the ice–snow sample and the surface of the copper cap, allowing for an isothermal boundary layer to form. A similar effect was observed and subsequently prevented in

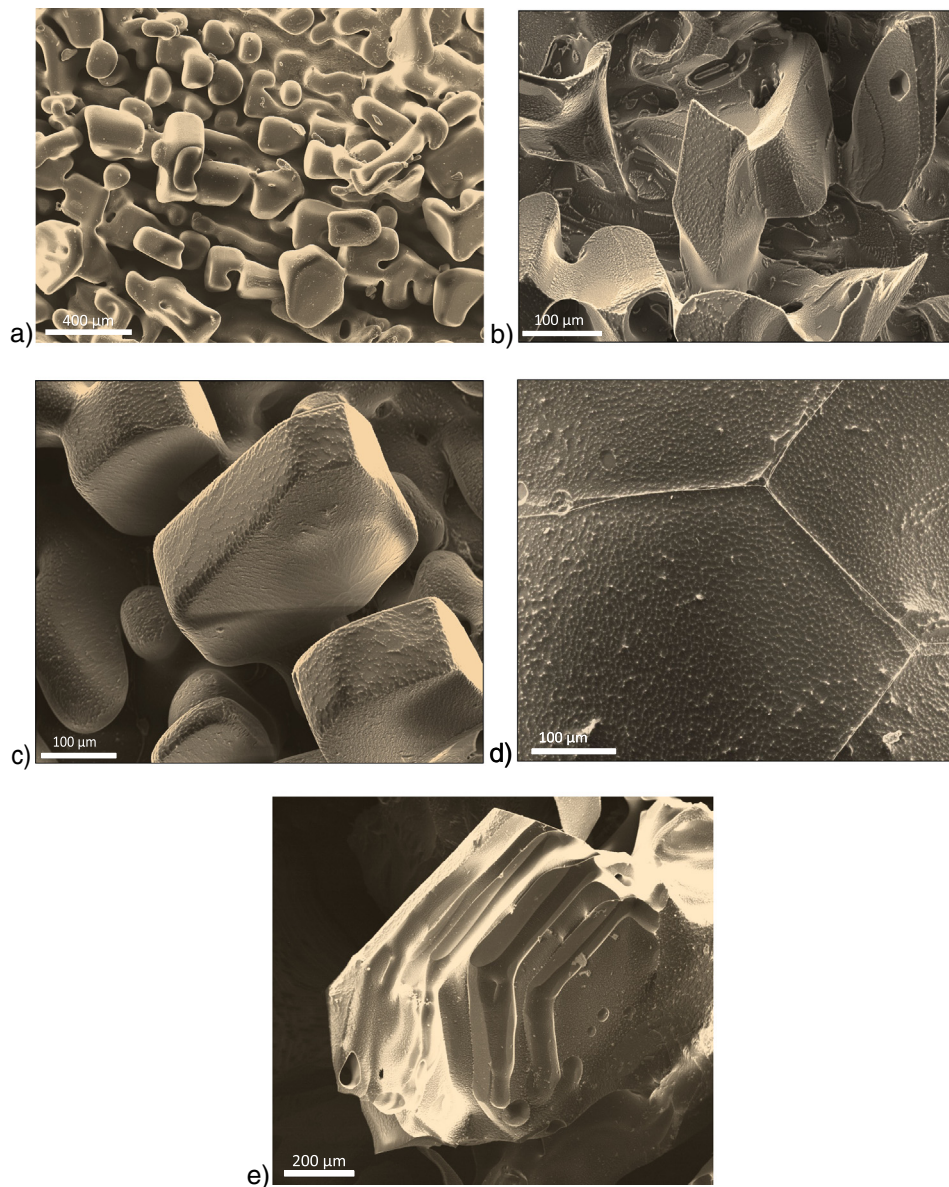


**Fig. 12.** ESEM images of (a) bottom of a 2 mm thick ice lens, (b) bottom of a 8 mm thick ice lens, (c) bottom of a 4 mm thick ice lens, (d) top of an 8 mm thick ice lens, and (e) a snow grain that was adjacent to the 8 mm thick ice lens after the 48 h period of an imposed  $-100 \text{ K m}^{-1}$  temperature gradient.

Pinzer et al. (2012), where a 4 mm thick ice lens was placed on the lower heat flux plate to prevent such a gap from forming during the application of a temperature gradient. Nevertheless, these results are thought to be of significance, as they would indicate for the first time via in situ measurements that a super-temperature gradient can exist near the interface of an ice lens and the adjacent snowpack.

Upon sequentially decreasing the imposed temperature gradient in our experiment (see Section 3.5), we observed that as the imposed temperature gradient was decreased, the overall magnitude of the local temperature gradient near the ice lens was also decreased, as shown in Fig. 14. In this plot, the error bars for each temperature gradient were calculated using the most conservative error estimate possible, as referenced in Section 3.5, where the spatial location of each thermocouple probe was allowed to vary by as much as  $\pm 200 \mu\text{m}$  in the z-direction. With this allowance, the  $\Delta Z$  used to calculate the temperature gradient can encompass a range of values from 0.6 mm to 1 mm. Despite this range for  $\Delta Z$ , the results indicate that at large temperature gradients ( $\geq 50 \text{ K m}^{-1}$ ) the observed temperature gradient below the ice lens is approximately 1.5–2 times greater than that above. Moreover,

these results also indicate that during the simultaneous decrease of these two temperature gradients, an inverse exponential relationship occurs. We describe this apparent phenomenon by taking the ratio, termed the Temperature Gradient Multiplier (TGM), of the observed to the imposed temperature gradient, given in Eq. (5).

$$\text{TGM} = \frac{\text{observed temperature gradient}}{\text{imposed temperature gradient}} \quad (5)$$

The TGM is plotted in Fig. 15 as a function of the imposed bulk temperature gradient. The utility of taking the TGM is that it shows that as the imposed bulk temperature gradient is decreased, the degree to which the local temperature gradient is greater than the imposed bulk temperature gradient increases inversely. This would indicate that even at very low ( $\leq -10 \text{ K m}^{-1}$ ) bulk measured temperature gradients, the local temperature gradient at the ice–snow interface may be many times greater than would have been previously thought via a more conventional field-based or continuum approach.

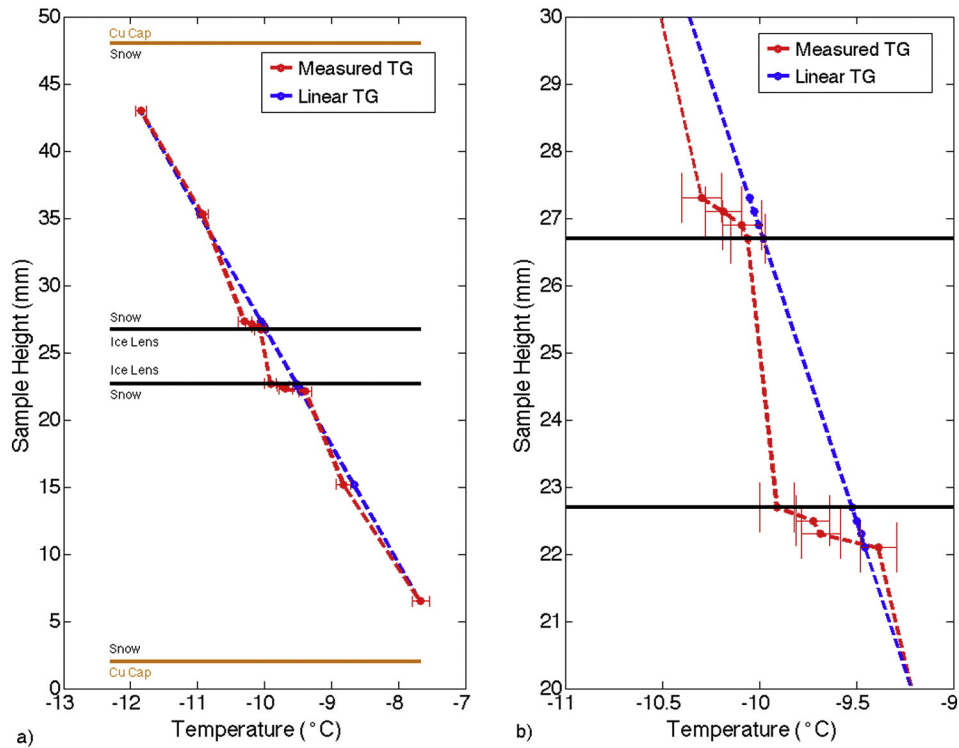


Fig. 13. Temperature gradient measurements around a 4 mm ice lens after steady state heat flow was achieved for (a) the entire sample, and (b) only over the 10 mm region of the sample containing the ice lens [enlargement of (a)].

5. Discussion

As shown in Fig. 13b, a dramatic temperature drop and increase in the temperature gradient was observed to occur both above and below the ice lens during conditions of steady-state heat flow. Should such a temperature drop also occur in natural snowpacks near similar thermal discontinuities, this would act to enhance kinetic snow metamorphism in that region. This sharp thermal discontinuity must be due to some combination of conductive, convective, or latent heat flow. Given that we can neglect the influence of both mass concentration and thermally induced convective boundary layers in our experiments (see Section 2.2), we turn our attention first to the contribution from pure conduction.

In a porous medium, such as snow, the temperature gradient through the material is controlled by the effective thermal conductivity

$k_{eff}$ , which accounts for the combination of the thermal conductivities of the solid (ice) and fluid (air) that fills the pore space (Bergman et al., 2011). From Riche and Schneebeli (2013), for snow of a similar shape, density, and SSA, we estimate the thermal conductivity of our snow sample  $k_{snow}$  to be near  $0.219 \text{ W m}^{-1} \text{ K}^{-1}$  (see their Table 1 in the Supplementary material, snow type: RGSr). This value is roughly a full order of magnitude greater than that of dry air ( $k_{air} = 0.024 \text{ W m}^{-1} \text{ K}^{-1}$  at 273 K, Wallace and Hobbs, 2006) and a full order of magnitude less than that of pure polycrystalline ice ( $k_{ice} = 2.4 \text{ W m}^{-1} \text{ K}^{-1}$  at 253 K, Petrenko and Whitworth, 1999). Such a discontinuity in thermal conductivities at the ice–snow interface would suggest thermal contact resistance as a contributing mechanism to the observed temperature drop, as illustrated in Fig. 16 (adapted from Cengel, 2007, see his

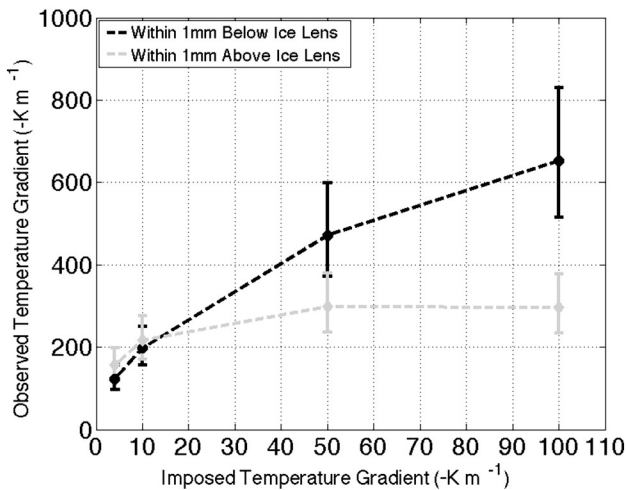


Fig. 14. Comparison of the imposed bulk temperature gradient to the local observed temperature gradient within 1 mm above and below the ice lens.

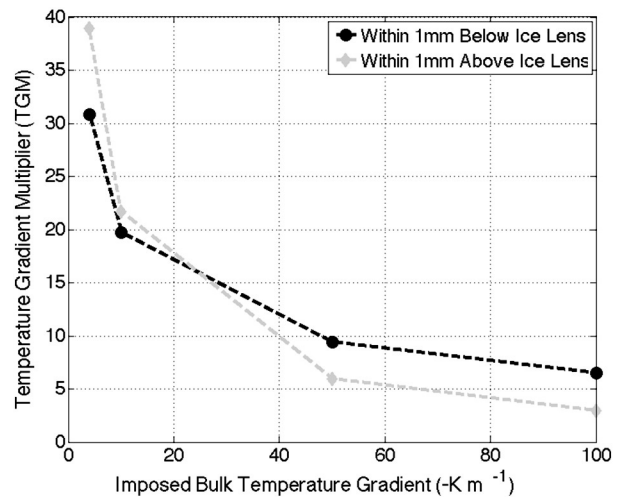


Fig. 15. TGM plotted as a function of the imposed bulk temperature gradient, illustrating an inverse relationship.

Figs. 3–14). Shown in this idealized representation, the conductive heat flow is ultimately limited by the number of connections that can exist between the snow and ice, which is itself limited by the size and shape of the snow grains, the roughness of the ice lens, and the porosity of the bulk snowpack at the interface. As the connectivity increases,  $k_{eff}$  also increases, which would then decrease the temperature gradient if conduction were the only heat transfer mechanism. Notice in Fig. 13a, that it is the highest thermal conductivity material (ice) that also has the smallest temperature gradient. As previously shown in Fig. 9,  $\rho_{conn}$  below the ice lens increases at a much faster rate than that above the ice lens, implying that the temperature gradient should be larger above the ice lens than that below, but this is not what we observed. Alternatively, in Section 4.2.4 and Fig. 11, the initial porosity below the ice lens was much greater than that of the bulk, but decreased over time. A decrease in the porosity at the interface could be perceived as analogous to an increase in the connectivity, which supports the former conclusion made in Fig. 9, but does not further elaborate on the factor of two differences in the temperature gradient above the ice lens as compared to below. In contemplating this difference, contributions from the latent heat flux must also be considered.

In some treatments of heat and mass transfer, contributions from the latent heat flux may also be included in  $k_{eff}$  (Greene, 2007). But in our experiments near the ice lens, it is not explicitly known whether the latent heat is being absorbed by the substrate (ice lens) upon deposition or being released into the pore space, effectively raising the temperature. When specifically addressing ice crystal growth from the vapor phase on a copper substrate, Shaw and Mason 1955 demonstrated that the latent heat is conducted away by the substrate. When grown from an icy substrate, Hobbs (1974) suggests that any variation from uniform linear growth would be due to variations in the surface temperature and that this would be directly related to the capacity of the substrate to conduct away the latent heat of deposition. Although we did not observe purely uniform ice crystal growth, we also did not observe any particularly abnormal ice crystal growth. However, if latent heat were being released into the pore space, we would expect to see 1) a drop in the surface temperature at the ice–snow interface above the ice lens where sublimation is occurring, 2) an increase in the temperature some distance away from the bottom of the ice lens where deposition is taking place, and 3) larger temperature gradients then would perhaps be predicted from conduction alone. When looking at Fig. 13b, this appears to be what is shown, suggesting that the release of latent heat into the pore space may be a contributing mechanism for enhancing the temperature gradient below the ice lens while decreasing the temperature gradient above the ice lens. When combining this effect with our observations of a higher porosity existing below the ice lens than above (see Fig. 11), this may explain the large difference in the temperature gradient between the two regions. In Part II of this

study, utilizing our in situ temperature measurements, we provide a more rigorous and quantitative analysis of the potential mechanisms responsible for heat and mass transfer at the ice–snow interface.

## 6. Conclusions

Under a controlled temperature gradient of  $-100 \text{ K m}^{-1}$ , we performed time-lapse in situ  $\mu$ -CT observations of a model snowpack containing artificially created ice lenses of 2 mm, 4 mm and 8 mm thickness. Subsequent to these observations, we examined each ice lens at high resolution using SEM. In a separate experiment, we made in situ temperature measurements from within 1 mm of the ice lens at temperature gradients of  $-100 \text{ K m}^{-1}$ ,  $-50 \text{ K m}^{-1}$ ,  $-10 \text{ K m}^{-1}$ , and  $-4 \text{ K m}^{-1}$ . The artificial construction of our model snowpack was implemented such that it would mimic natural conditions. We found that:

- i. Local temperature gradients on a sub-millimeter scale above and below the ice lens can be nearly 40 times larger than the macroscopic imposed temperature gradient.
- ii. New ice crystal growth via deposition on the bottom face of the ice lens occurs simultaneously with sublimation from the top surface.
- iii. The local temperature gradient below the ice lens was found to be greater than above the ice lens for imposed temperature gradients larger than  $-10 \text{ K m}^{-1}$ .
- iv. Kinetic snow metamorphism and subsequent weak layer development near the ice–snow interface may be enhanced by temperature gradients much larger than what may be detectable with field-based instrumentation.

Although we contend that the work presented here has taken an important step in further comprehending the dramatic effects that an ice lens may have on an otherwise homogeneous snowpack, we acknowledge that a more rigorous analysis of our results still remains necessary. This is the focus of Part II of this study.

## Acknowledgments

This work was supported by the Theo Meiners Research Grant awarded on behalf of the American Avalanche Association, the National Science Foundation grant number PLR 1141411, and the U.S. Army Corps of Engineers, Cold Regions Research and Engineering Laboratory. The authors acknowledge the use of the Ice Research Laboratory (Director E.M. Schulson) at the Thayer School of Engineering. We thank Zoe Courville for her procurement of equipment and

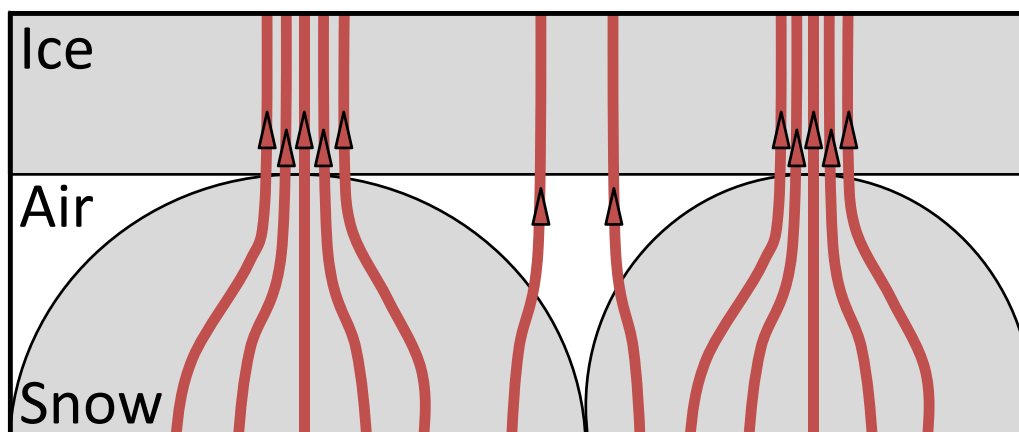


Fig. 16. Idealized representation of the conductive heat flow at the interface between a solid layer of ice and a porous layer of snow.

experimental input. We thank Rachel Obbard and Scott Snyder for their help with SEM imaging and natural snow collection.

## Appendix A. Supplementary data

Supplementary data to this article can be found online at <http://dx.doi.org/10.1016/j.coldregions.2015.09.006>.

## References

- Adams, E.E., Brown, R.L., 1983. Metamorphism of dry snow as a result of temperature gradient and vapor density differences. *Ann. Glaciol.* 4, 3–9.
- Adams, E.E., Brown, R.L., 1990. A mixture theory for evaluation heat and mass transport processes in nonhomogeneous snow. *Contin. Mech. Thermodyn.* 2, 31–63.
- Akitaya, E., 1974. Studies on depth hoar. *Contributions from Institute of Low Temperature Science. Ser. A* 26, 1–67.
- Armstrong, R.L., 1985. Metamorphism in a Subfreezing, Seasonal Snow Cover: The Role of Thermal and Vapor Pressure Conditions, Ph.D. Dissertation. University of Colorado (175 pp.).
- Bergman, T.L., Lavine, A.S., Incropera, F.P., Dewitt, D.P., 2011. *Fundamentals of Heat and Mass Transfer*. John Wiley and Sons 1048 pp.
- Birkeland, K.W., Johnson, R.F., Schmidt, D.S., 1998. Near-surface facet crystals formed by diurnal recrystallization: a case study of weak layer formation in the mountain snowpack and its contribution to snow avalanches. *Arct. Alp. Res.* 30 (2), 200–204.
- Cengel, Y.A., 2007. *Heat and Mass Transfer: A Practical Approach*. McGraw Hill, Third Edition 901 pp.
- Chen, S., Baker, I., 2010. Structural evolution during ice-sphere sintering. *Hydrol. Process.* 24, 2034–2040.
- Colbeck, S.C., 1991. The layered character of snow covers. *Rev. Geophys.* 29, 81–96.
- Colbeck, S.C., Jamieson, J.B., 2001. The formation of faceted layers above crusts. *Cold Reg. Sci. Technol.* 33, 247–252.
- Cole, D.M., 1979. Preparation of polycrystalline ice specimens for laboratory experiments. *Cold Reg. Sci. Technol.* 1, 153–159.
- Fierz, C., 1998. Field observations and modelling of weak-layer evolution. *Ann. Glaciol.* 26, 7–13.
- Fierz, C., Armstrong, R.L., Durand, Y., Etchevers, P., Greene, E., McClung, D.M., Nishimura, K., Satyawali, P.K., Sokratov, S.A., 2009. The international classification for seasonal snow on the ground. IHP-VII Technical Documents in Hydrology No. 83, IACS Contribution No. 1. UNESCO-IHP, Paris (80 pp.).
- Flin, F., Brzoska, J.B., 2008. The temperature-gradient metamorphism of snow: vapour diffusion model and application to tomographic images. *Ann. Glaciol.* 49 (1), 17–21.
- Ghiaasiaan, S.M., 2011. *Convective Heat and Mass Transfer*. Cambridge University Press 524 pp.
- Greene, E.M., 2007. The Thermophysical and Microstructural Effects of an Artificial Ice Layer in Natural Snow Under Kinetic Growth Metamorphism. Ph.D. Dissertation. Colorado State University (147 pp.).
- Greene, E., Johnson, G., 2002. Characterization of a deep slab instability. *Proceedings of the International Snow Science Workshop*, Penticton, BC, pp. 491–498 (October 2002).
- Hobbs, P.V., 1974. *Ice Physics*. Clarendon Press, Oxford 837 pp.
- Holman, J.P., 2002. *Heat Transfer*. McGraw Hill 665 pp.
- Jamieson, B., Johnston, C., 1997. The facet layer of November 1996. *Avalanche News* 52, 10–15.
- Jamieson, B., Geldsetzer, T., Stethem, C., 2001. Forecasting for deep slab avalanches. *Cold Reg. Sci. Technol.* 33, 275–290.
- Jennings, S.G., 1988. The mean free path in air. *Journal of Aerosol Science* 19. Elsevier, pp. 159–166 (2).
- Kaempfer, T.U., Schneebeli, M., Sokratov, S.A., 2005. A microstructural approach to model heat transfer in snow. *Geophys. Res. Lett.* 32, 1–5.
- Kakac, S., Yener, Y., 1993. *Heat Conduction*. Taylor & Francis 363 pp.
- Levenspiel, O., 1998. *Engineering Flow and Heat Exchange*. Springer 378 pp.
- Libbrecht, K.G., 2004. A critical look at ice crystal growth data. Cornell University Library (arXiv:cond-mat/0411662 [cond-mat.mtrl-sci]).
- Löwe, H., Van Herwijnen, A., 2012. A Poisson shot noise model for micro-penetration of snow. *Cold Reg. Sci. Technol.* 70, 62–70.
- Marshall, H.P., Johnson, J.B., 2009. Accurate inversion of high-resolution snow penetrometer signals for microstructural and micromechanical properties. *J. Geophys. Res. Earth Surf.* 114.
- McClung, D., Schaerer, P., 2006. *The Avalanche Handbook*. The Mountaineers, Seattle 342 pp.
- Petrenko, V.F., Whitworth, W., 1999. *Physics of Ice*. Oxford University Press 373 pp.
- Pinzer, B., Schneebeli, M., Kaempfer, T., 2012. Vapor flux and recrystallization during dry snow metamorphism under a steady temperature gradient as observed by time-lapse micro-tomography. *The Cryosphere* 6, 1141–1155.
- Powers, D.J., O'Neill, K., Colbeck, S.C., 1985. Theory of natural convection in snow. *J. Geophys. Res.* 90 (B6), 641–649 (10).
- Pruppacher, H.R., Klett, J.D., 1997. *Microphysics of Clouds and Precipitation*. 2nd Ed. Kluwer Academic Publishers (954 pp.).
- Riche, F., Schneebeli, M., 2013. Thermal conductivity of snow measured by three independent methods and anisotropy considerations. *The Cryosphere* 7, 217–227.
- Schirmer, M., Jamieson, B., 2014. Limitations of using a thermal imager for snow pit temperatures. *The Cryosphere* 8, 387–394.
- Schneebeli, M., Sokratov, S.A., 2004. Tomography of temperature gradient metamorphism of snow and associated changes in heat conductivity. *Hydrol. Process.* 18 (18), 3655–3665.
- Schweizer, J., Kronhom, K., Jamieson, J.B., Birkeland, K.W., 2008. Review of spatial variability of snowpack properties and its importance for avalanche formation. *Cold Reg. Sci. Technol.* 51 (2–3), 253–272.
- Shea, C., Jamieson, B., Birkeland, K.W., 2012. Use of a thermal imager for snow pit temperatures. *The Cryosphere* 6, 287–299.
- Shertzer, R.H., Adams, E.E., 2011. Anisotropic thermal conductivity model for dry snow. *Cold Reg. Sci. Technol.* 69, 122–128.
- Sobhan, C.B., Peterson, G.P., 2008. *Microscale and nanoscale heat transfer. Fundamentals and Engineering Applications* (409 pp.).
- Sturm, M., Johnson, J.B., 1991. Natural convection in the subarctic snow cover. *J. Geophys. Res.* 96 (B7), 657–671 (11).
- Wallace, J.M., Hobbs, P.V., 2006. *Atmospheric Science: An Introductory Survey*. Elsevier (483 pp.).
- Wang, X., Baker, I., 2014. Evolution of the specific surface area of snow during high temperature gradient metamorphism. *J. Geophys. Res.-Atmos.* 119 (24), 13690–13703.